Research Article | Vol. 26, No. 22 | 29 Oct 2018 | OPTICS EXPRESS 28441
Optics EXPRESS

Single-shot nanosecond-resolution multiframe passive imaging by multiplexed structured image capture

MARK GRAGSTON,[1] CARY SMITH,[1] DANIIL KARTASHOV,[2] MIKHAIL N. SHNEIDER,[3] AND ZHILI ZHANG[1,*]

[1]*Mechanical, Aerospace, and Biomedical Engineering, University of Tennessee, Knoxville, TN 37996, USA*
[2]*Institute for Optics and Quantum Electronics, Friedrich-Schiller-University Jena, 07743 Jena, Germany*
[3]*3Mechanical and Aerospace Engineering, Princeton University, Princeton, NJ 08544, USA*
**zzhang24@utk.edu*

Abstract: The Multiplexed Structured Image Capture (MUSIC) technique is used to demonstrate single-shot multiframe passive imaging, with a nanosecond difference between the resulting images. This technique uses modulation of light from a scene before imaging, in order to encode the target's temporal evolution into spatial frequency shifts, each of which corresponds to a unique time and results in individual and distinct snapshots. The resulting images correspond to different effective imaging gate times, because of the optical path delays. Computer processing of the multiplexed single-shot image recovers the nanosecond-resolution evolution. The MUSIC technique is used to demonstrate imaging of a laser-induced plasma. Simultaneous single-shot measurements of electron numbers by coherent microwave scattering were obtained and showed good agreement with MUSIC characterization. The MUSIC technique demonstrates spatial modulation of images used for passive imaging. This allows multiple frames to be stacked into a single image. This method could also pave the way for real-time imaging and characterization of ultrafast processes and visualization, as well as general tracking of fast objects.

© 2018 Optical Society of America under the terms of the OSA Open Access Publishing Agreement

1. Introduction

Passive imaging at nanoseconds or less exposure time has many scientific and engineering applications, including laser-material interactions, femtosecond filament, high harmonic generations, ultrafast chemistry, and air lasing [1]. Current complementary metal-oxide semiconductor (CMOS) and charge-coupled device (CCD) imaging devices cannot reach this speed due to limited on-chip storage capacity and electronic readout speeds, although in theory silicon can reach sub-nanosecond speed [2,3]. Various optical gating and pump-probe approaches, such as ultrashort pulse interference [4], the Kerr electro-optic effect for ballistic imaging [5,6], can capture only a single image. Temporal scanning, i.e., repetitive measurements with a varied delay between the pump and probe or between laser pulse and camera gate can be used [7], but are significantly limited the applications to repetitive events, and therefore, only provide statistical measurements. Recent demonstrations of passive imaging methods utilize compressed sensing to recover ultrafast images from a streak camera or temporal pixel multiplexing [8], which is different from the current approach [9,10]. Others have utilized spatial modulation of the light source for boosting imaging speeds and storing multiple images in a single frame [11]. Modulation of light just prior to collection for boosting imaging speeds has also been demonstrated [12,13]. A recent review [14] explores in detail a variety of novel ultra-fast single-shot imaging techniques.

In the present work, a detailed study of single-shot, passive imaging with temporal resolution at the nanosecond level is presented using a unique high-speed computational

#345586 https://doi.org/10.1364/OE.26.028441
Journal © 2018 Received 14 Sep 2018; revised 10 Oct 2018; accepted 10 Oct 2018; published 17 Oct 2018

Optics EXPRESS

imaging method, namely Multiplexed Structured Image Capture (MUSIC). As a passive imaging method, MUSIC encodes the temporal evolution of the scenes in a single snapshot into spatial frequency shifts; thus, producing multiplexed images. These multiplexed images contain image information from several points in time, which can be separated computationally. Furthermore, MUSIC can essentially bypass the speed limits of electronic and/or mechanical shutters in the high-speed cameras since the encoding is done optically. In this current form of MUSIC, modulation patterns are applied just before imaging. Sub-exposure 2D images corresponding to the optical flight time of nanoseconds are demultiplexed and extracted, revealing nanosecond evolution of the 2D scene in the post processing. In theory, the MUSIC method might extend the single-shot passive imaging up to femtoseconds, which will provide an alternate approach for ultrafast passive imaging and unprecedented insights on ultrafast physics and chemistry. Theoretical limitations on maximum multiplexed patterns are discussed as combinations of diffraction limits and spatial resolutions of the recovered images.

Laser-induced ionization and plasma is used as an imaging target. It has been widely used for various applications ranging from basic scientific laboratories to space exploration, including femtosecond filament [15], high harmonic generation [16], air lasing [17], Laser-induced Breakdown Spectroscopy (LIBS) [18–20], laser-induced ignition [21] and etc. Laser plasma generation begins with the creation of seed electrons from multiphoton ionization and/or Keldysh tunneling ionization processes near the laser focal position by the front end of the high-intensity pulse, with the latter mechanism only becoming applicable for very high intensities. For the ns-pulse used in this work, non-resonant multiphoton ionization is the seed electron generation mode. The seed electrons absorb a large percentage of the remaining laser pulse and are accelerated by the laser's electromagnetic field via the inverse-bremsstrahlung effect. With a sufficient optical field applied, the electrons are accelerated to energies sufficient for electron impact ionization upon collisions with the neutral gas atoms and molecules. The newly liberated electrons are then accelerated by the field leading to an electron avalanche ionization process during the laser pulse in nanoseconds [22,23]. The development of the laser plasma is a very dynamic process, and plasma parameters can change drastically within a nanosecond considering that electron collisions are on the order of tens of picoseconds. Therefore, the LIBS plasma is used as a target for high-speed imaging.

2. Experiment setup

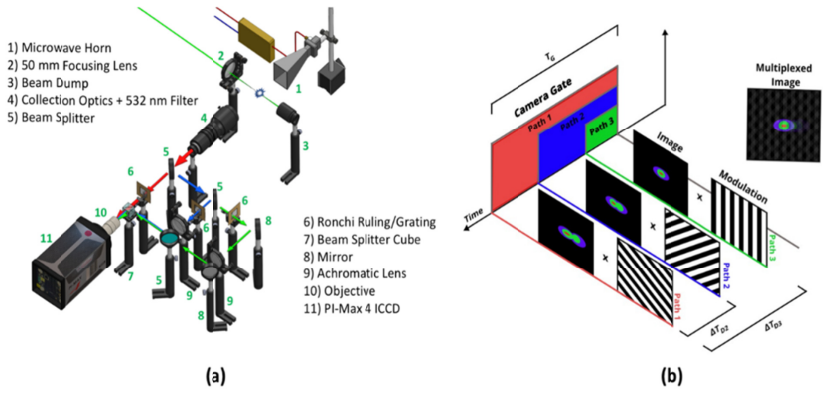


Fig. 1. (a) Schematics of the experiment setup for simultaneous measurements of laser-induced avalanche ionization by coherent microwave scattering and three-channel MUSIC. (b) Timing diagram for nanosecond-resolution MUSIC at three individual channels. Each path is modulated with unique patterns by Ronchi rulings (component 6 in (a)). The time of flight along each path is distinct so that time-multiplexed images from the plasma can be captured into a single snapshot, shown on the top. The time axis shows how much of the event

Optics EXPRESS

information was captured in each channel. Note that path 3 contributes information from the earliest times only.

2.1 Three-channel multiplexed structured image capture (MUSIC) system

A variable zoom camera lens was used to relay the plasma emissions. The first beam splitter (30% transmission, 70% reflection) was used to separate the images into the path one, path two, and path three. The image was further split by the second beam splitter (50% transmissions, 50% reflection) into path two and three. The plasma image was projected onto three Ronchi rulings (10 grooves per millimeter) along three optical paths. The modulated images were merged by a beam combiner cube before being collected by a gated Intensified CCD camera (Princeton Instruments, PI Max 4). The optical paths along three channels are 10 cm, 40 cm, and 70 cm, respectively, which corresponds to 1 ns of delay for path two and 2 ns of delay for path three relative to the path one. The number of channels can be expanded as needed to extend more simultaneous imaging. The MUSIC system, as an ultrafast imaging system, can be used for single-shot nanosecond resolution or higher imaging and measurements of laser-induced plasma generation and visualization and tracking of fast objects.

2.2 Coherent microwave scattering system

A 10-dBm tunable microwave source (HP 8350B sweep oscillator, set at ~10 GHz) was split into two channels [22,24]. One of the channels was used to illuminate the plasma by employing a microwave horn (WR75, 15-dB gain). The backscattering is monitored through a homodyne transceiver detection system. The scattering from the plasma is collected by the same microwave horn. The signal passes through a microwave circulator and is amplified 30 dB by one preamplifier at ~10 GHz. After the frequency is down-converted with by mixing with the second channel, two other amplifiers with bandwidth in the range 2.5 kHz – 500MHz amplifies the signal 60 dB. Considering the geometry of dipole radiation of microwave, the polarization of the microwave is chosen to be along the propagation direction of the laser beam, maximizing the scattering signal. The coherent microwave scattering system can be used to monitor the generation and evolution of electrons in the laser-induced plasma region with a temporal resolution of ~3 ns.

2.3 Imaging target

532 nm laser radiation from an Nd:YAG laser (Continuum Surelite) operating with a nominal 8 ns pulse width at 10 Hz repetition rate was focused with a 50mm plano convex lens into a 20μm spot, yielding the peak intensity of ~10^{12} W/cm^2. Coherent microwave scattering and MUSIC were used to simultaneously characterize the laser-induced ionization in air, as shown by the experiment setup in Fig. 1(a). Microwave scattering can measure the total electron number evolution with a temporal resolution of ~3 nanoseconds (ns). Note that plasma expansion leads to a critical electron number density beyond the microwave penetration depth, which causes the microwave signal to decrease after peak [22].

A variable zoom camera lens was used to relay the plasma emissions into the three-channel MUSIC apparatus, as shown in Fig. 1(a). The MUSIC apparatus for this work consists of two parts, the optical delay circuits and the spatial modulation component in each delay circuit. Beam splitters and mirrors allow for plasma emissions to travel three different paths, each of which encodes the image with a different spatial modulation pattern. An intensified camera (Princeton Instruments PIMax 4) with a gate width of 3 ns was used to collect the combined images out of the MUSIC apparatus. Note that the gated camera can only collect light over a time equal to the gate width, T_G. The information from path one was modulated and sent to the camera after the beam splitter and contributes image information during the entire gate width. The same image was then split and modulated repeatedly, each time causing a delay relative to the start of the camera exposure gate, as shown in Fig. 1(b).

Optics EXPRESS

Thus, the delayed modulated images arrived later at the camera due to time of flight differences. Since images from each path were modulated differently, each image can be individually demultiplexed and recovered. Furthermore, since each image contained the same information but was imaged for different exposure times, delayed images represent earlier time information in accordance with Fig. 1(b).

It should be noted that the current configuration uses beamsplitters and optical delays to gain the temporal resolutions among multiplexed images. The advantages are the simplicity in the experimental setup: optical delays can be on the order of picoseconds or femtoseconds for higher temporal resolutions. While it leads to a reduced optical efficiency for adding more channels.

3. Results

3.1 Imaging model

The multiplexed image intensity, I_{CAM}, collected by the camera in multiple channels is

$$I_G(\bar{r},t)=\sum_{n=1}^{3}W(t)I_n\left(\bar{r},t-\Delta t_{Dn}\right)M_n\left(\bar{r}\right)\varepsilon_n \tag{1}$$

where $\Delta t_{Dn}=t_{Dn}-t_{D1}$ is the time delay that has traveled path n relative to path one and I_n is the image intensity traveling along path,

$$I_n\left(\bar{r},t-\Delta t_{Dn}\right)=\begin{cases}0 & t<\Delta t_{Dn}\\ I\left(\bar{r},t\right) & t\geq\Delta t_{Dn}\end{cases} \tag{2}$$

Here, $I\left(\bar{\boldsymbol{r}},t\right)$ is the image intensity, $M_n\left(\bar{\boldsymbol{r}}\right)$ is the spatial modulation mask for path n, and ε_n is the optical efficiency of path n. Imaging with a gated camera can be modeled as windowing in the time domain, integrating (i.e. summing) image intensity over the window, and sampling in the spatial domain, with the spatial sampling determined by the pixel layout and size. The windowing function is a square pulse centered at time t_0 with width T_G,

$$W\left(t\right)=\Pi\left(\frac{t-t_0}{T_G}\right)=\begin{cases}0 & |t|>\frac{1}{2}\\ \frac{1}{2} & |t|=\frac{1}{2}\\ 1 & |t|<\frac{1}{2}\end{cases} \tag{3}$$

and $t_0=T_{GD}+T_G/2$, with T_{GD} denoting the gate delay time.

Each term in the sum in Eq. (1) represents image information that has traveled at a different path. Since the camera gate is finite in time, information delayed by traveling different paths is sliced and shortened by the gate, effectively giving the delayed information shorter gate times, i.e., time of flight acquisition. The spatial modulation resulting from applying a unique mask $M_n\left(\bar{\boldsymbol{r}}\right)$ to each path, which is multiplication of the images with the masks in the spatial domain, is equivalent to the convolution of the images and masks in the spatial frequency domain. The Ronchi rulings used in this work to apply the modulation patterns are modeled as periodic square waves with spatially frequency k_0.

Optics EXPRESS

In the spatial frequency domain, the multiplexed image can be shown as,

$$\tilde{I}_G\left(\bar{k},t\right)=\Pi\left(\frac{t-t_0}{T_G}\right)\sum_{n=1}^{3}[\varepsilon_n I_n\left(\bar{k},t-\Delta t_{Dn}\right)\otimes\sum_{m=-\infty}^{\infty}\frac{2\sin\left(mk_0T_1\right)}{m}\delta\left(k_{xn}^{'}-mk_0\right)] \quad (4)$$

Here "$\otimes$" denotes the convolution operator, where the right-hand side comes from the Fourier transform of the Ronchi ruling pattern, and $k_{xn}^{'}=k_x\cos\theta_n+k_y\sin\theta_n$. Rotation of the Ronchi ruling by angle θ_n rotates the Fourier transform of the mask by the same amount, which is a sinc function.

Images through each path contribute a unique shifted spatial frequency throughout the gate time T_G due to $k_{xn}^{'}$ being different, which is shown in Fig. 2(a). It implies that due to the Dirac delta function in Eq. (4), each harmonic of the sinc function in the spatial frequency domain of the masked image contains a copy of the image of the Fourier transform of the pre-masked image. Therefore, most of the image information is uniquely preserved in the in higher harmonics shown in Fig. 2(a), and by using Ronchi rulings with different rotations for each path, this information can be kept separate in the final composite image even if there is significant image overlap. Note that the center of the Fourier domain represents unshifted DC components of the information, and therefore contains information from all three paths.

3.2 Computational image recovery

The fundamental principle of MUSIC in this application is to encode the time lapse into the spatial frequency domain, thereby allowing a single, cumulative exposure to be captured that contains multiple individual images (the maximum number of images than can be stored is discussed later in this work). The encoded images are then recovered through selective filtering in the frequency domain. The spatial resolution of the multiplexed images is reduced and dependent on the bandwidth of the low-pass filter used during recovery. It is inherently determined by the uncertainty principle of Fourier transformation, i.e., $\Delta f_r\cdot\Delta r\geq 1$. Furthermore, it should be noted that the spatial frequencies of most images lie within low frequency ranges as discussed in compressed sensing techniques [25]. A loss of <5% of high spatial frequency components is generally used as the criterion for recovery.

Optics EXPRESS

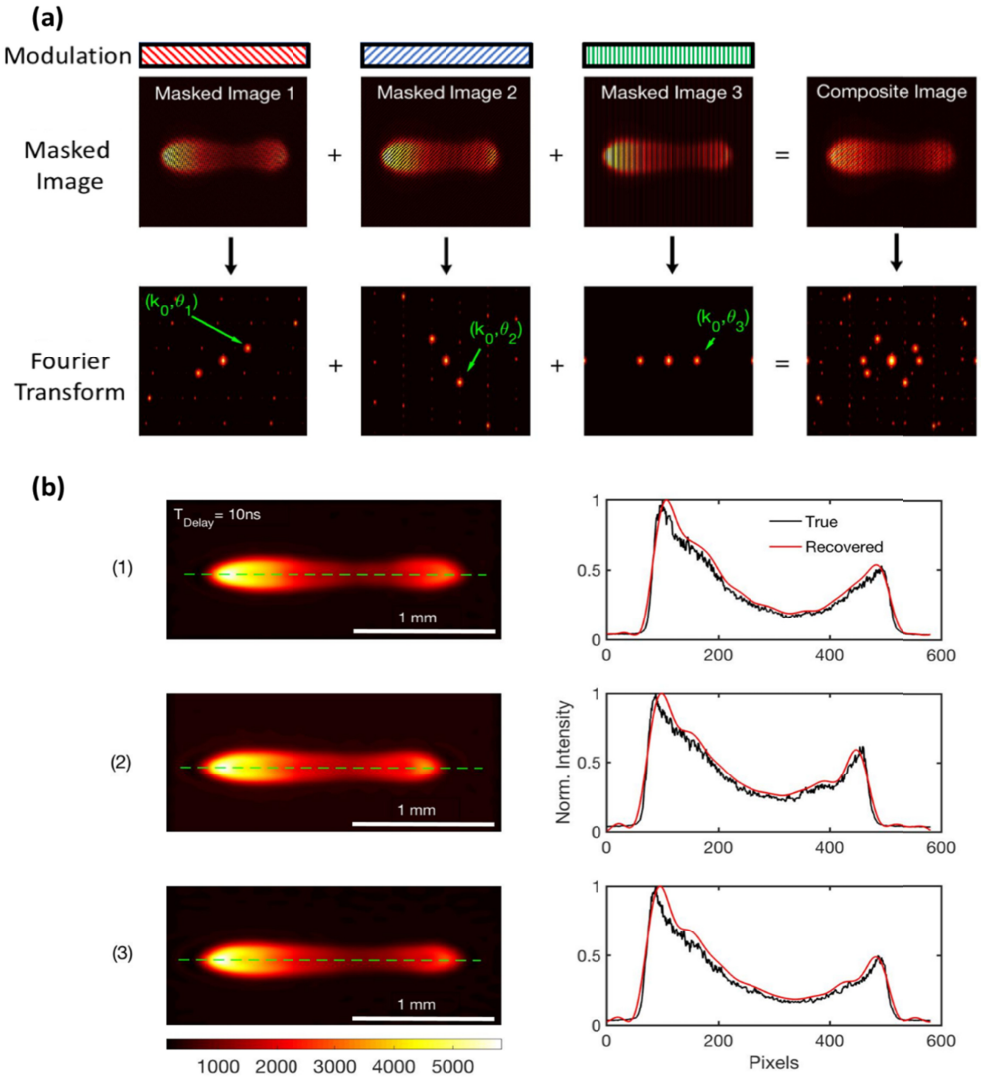


Fig. 2. (a) Phantoms of multiplexing of plasma emission by various spatial frequency modulations are shown as individual modulated images as Masked Image 1, 2, and 3 and the resulting multiplexed composite image. Each of the three images has a mask applied to it via multiplication and is summed into a composite multiplexed image, which represents the image stored by the camera during the gate time. The Fourier transform of each image is shown underneath, specifically showing that the Fourier transform of the composite image is equivalent to summing the Fourier transforms of each individual image. Arrows indicate the first harmonic of the sinc function. (b) Computational images recovered from the composite image in (a) and a line profile comparison to the true image before applications of masks.

Computational image recovery on the phantoms of multiplexed plasma emissions was conducted. A two-step recovery was used: first shifting the corresponding harmonic back to the center of the spatial frequency domain was to remove the modulation patterns from the multiplexed images and then applying a low-pass filter around the center region was to recover individual images, which is similar to methodology used for structured illumination technique [12]. The size of the filter determines the resolution, since any spatial information outside the filter is lost; however, the filter size must also be small enough to prevent interference from other harmonics in the Fourier domain. Figure 2(b) shows the recovered

Optics EXPRESS

images from the composite image in Fig. 2(a). Comparisons of line profiles from original phantom with the ones from the recovered images show very good agreement.

3.3 Experimental image recovery

Experimental demonstration of single-shot nanosecond-resolution imaging of laser-induced plasma was conducted, as shown in Fig. 1(a). The optical paths from the first beam splitter to the beam combiner are 10 cm, 40 cm, and 70 cm for path one, two and three, respectively. It leads to the difference of time of flight are 1.2 ns for path two and 2.8 ns for path three, compared to path one, i.e., achieving ~1 nanosecond temporal resolution between measurements. Figure 3(a) shows an example of a single-shot multiplexed image of the plasma emission by the three-channel MUSIC system with laser energy of ~60mJ/pulse, camera gate delay of 4.0 ns after the laser pulse, and camera gate width of 3.0 ns. The corresponding Fourier transformation in Fig. 3(b), demonstrates that each path has contributed information to the multiplexed image in a similar manner to phantoms in Fig. 2(b). Depending on relative image intensities from various paths, the higher-harmonics, which result from the square wave modulation by the Ronchi ruling, are shown and well-separated in the Fourier domain.

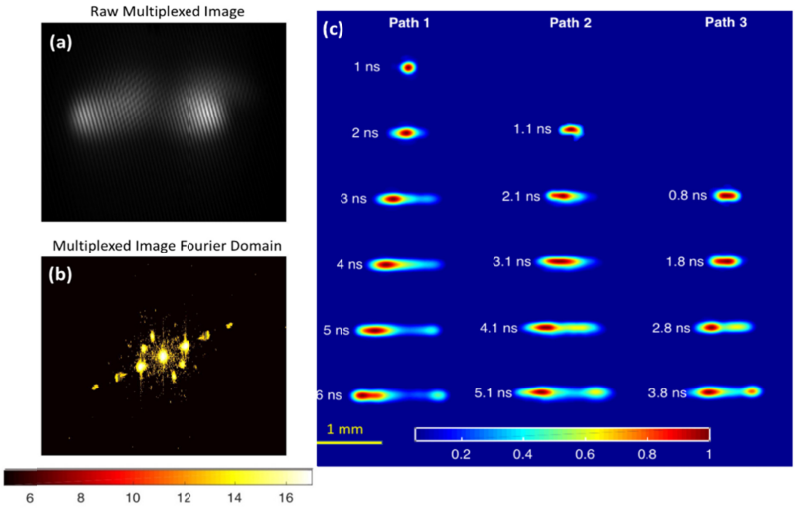


Fig. 3. (a) Experiment image of laser-induced plasma with all three channels present and the associated Fourier transform showing the multiplexing. Camera gate delay was set at 4ns with a gate width of 3ns. (b) Fourier transformation of (a), showing multiple modulated spatial frequency components from various optical paths. (c) Recovered images of laser-induced plasma using MUSIC. Note that each row is a single shot. Path one, two, and three have effective camera gate widths of 3.0 ns, 2.1 ns, and 0.8 ns respectively. (Left) Laser power was 60 mJ/pulse with an 8 ns pulse width and repetition rate of 10 Hz. A 50 mm focusing lens was used to generate the plasma.

Figure 3(b) shows a group of recovered images, three per laser shot, of the laser-induced plasma by different laser pulses. Images from each row were recovered from the same laser shot and captured within a single camera gate of 3.0 ns. On the first row, the plasma appeared in path one first as the camera gate starts at 2.0 ns ahead of the laser pulse. Significant ionization occurred in the last nanosecond of the gate. Subsequently on the second row, the plasma emissions showed on path one and two, as the camera gate started at 1.0 ns ahead of the laser. The rest of the images showed the sequential move of the camera gate by 1.0 ns on each row. Single-shot imaging of laser-induced plasma emissions was obtained at ~1 nanosecond. It should be noted that reduction of optical delay paths can lead to even faster

Optics EXPRESS

imaging of the plasma, thus the MUSIC method is only limited by the number of modulation patterns and available photons for imaging. For example, a delay of hundreds of microns would produce ultrafast imaging at petahertz. The recovery of the multiplexed images will need to be subtracted to remove the temporal overlaps.

3.4 Comparisons with coherent microwave scattering and plasma modeling

To get insight into the physics of laser-induced ionization and the time scales associated with its evolution, comparisons of the MUSIC measurements with coherent microwave scattering and numerical simulations solving the Boltzmann kinetic equation for the electron energy distribution function (EEDF) were conducted. Emissions from laser-induced plasmas are initially broadband continuum as inverse bremsstrahlung and free-free transitions . The emissions become distinct atomic emission lines after the plasma cools down at 20 - 30 ns [22]. Coherent microwave scattering tracks total electron number in the plasma and is proportional to the total plasma emissions in the avalanche phase of the plasma generation. It should be noted that our emphasis here is a qualitative comparison of microwave scattering, MUSIC and plasma modeling to confirm temporal evolution of the plasma.

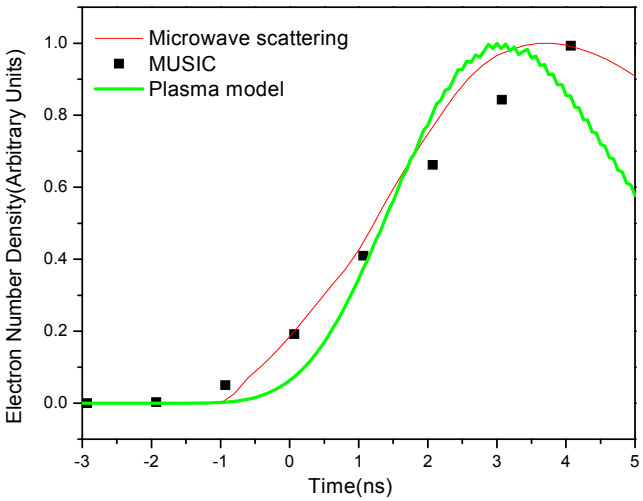


Fig. 4. Comparison of total image intensity of recovered images to microwave scattering and plasma modeling of the laser-induced plasma. The red solid line shows a convolution of the kinetic simulation results with the response function of the microwave diagnostic.

The plasma kinetic model is based on a non-stationary kinetic equation under Lorentz approximation and includes effects of collisional electron heating by the laser field, generation of new electrons in the process of optical field ionization (OFI) from the ground and electronically excited molecular states, elastic scattering of electrons on N_2 and O_2 molecules in air, inelastic processes of electron impact excitations of the $A^3\Sigma_u$, $B^3\Pi_g$, $a^1\Sigma_u$, $a^1\Pi_g$, $C^3\Pi_u$ electronic states in molecular nitrogen, vibrational excitation in N_2 and O_2 molecules, and electron impact ionization from the ground and excited electronic states. The calculated EEDF provides reaction rates for the coupled set of balance equations for the densities of electrons, neutral, and ionic and electronically excited molecular and atomic species. The OFI source of electrons is described using Popov-Perelomov-Terent'ev (PPT) strong field ionization model [26] in the form suggested in [27] and the photoelectron energy distribution function derived in [28]. The calculations start 3 ns before the maximum of the laser pulse when the OFI generated electron density reaches 10^{10} cm^{-3}. The plasma density predicted by the simulations reaches the value $\approx 6 \cdot 10^{17}$ cm^{-3} which is in a very good

Optics EXPRESS

agreement with the value ≈$7.5 \cdot 10^{17}$ cm^{-3} retrieved from the coherent microwave scattering measurements [23].

Figure 4 shows a comparison of the MUSIC measurements with the coherent microwave scattering and the simulated evolution of the plasma electron density. The results are normalized to show the overall temporal evolution only, since the plasma emissions from MUSIC measurements are proportional to total electron number without absolute calibration. Additionally, it should be noted that measured values are the result convoluted with an instrument function having a temporal resolution ~1 ns, which leads to the discrepancies at the initial phase of the ionization.

Optics EXPRESS

4. Discussion: maximum number of multiplexing patterns and resolution limitations

As shown in Figure 5, there is a theoretical limit for multiplexing single exposure, which is determined by the desired spatial resolution and imaging system diffraction limits. The maximum multiplexing is determined by first considering the maximum resolution desired for each recovered image, which has a corresponding spatial frequency, k_{filter}. This k_{filter} is used as the filter radius in the Fourier domain during image recovery. Furthermore, note that the only space available in the Fourier domain to shift image information to is the annulus defined between k_1, a spatial frequency cutoff of the common fundamental harmonic, and k_{diff}, the spatial frequency corresponding to the diffraction limit. Then an upper bound on the number of patterns that can be used in the multiplexing, N_u, is the ratio the area of the annulus, $A_{Annulus}$, in the Fourier domain to the area of the filter, A_{Filter}:

$$A_{Filter} = \pi k_{filter}^2 \tag{5}$$

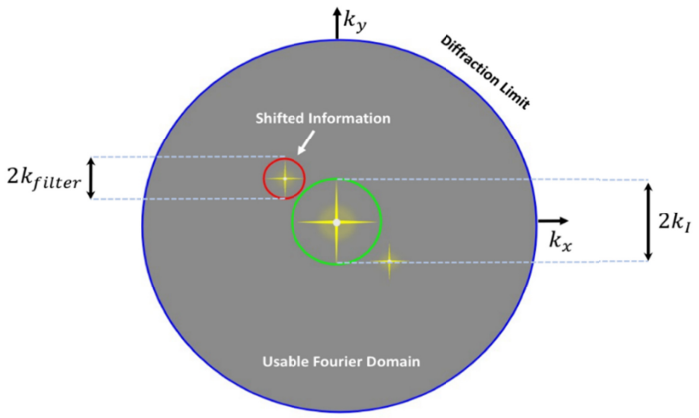


Fig. 5. The ultimate boundary is the spatial frequency associated diffraction limit of the system. However, low frequency information common to all images regardless of modulation (i.e. the fundamental harmonic) must be avoided too. Therefore, the space available to store the modulated image data is an annulus.

In the spatial frequency domain (i.e., Fourier domain), the radius of diffraction limit of the system can be expressed as

$$A_{Annulus} = \pi\left[k_{diff}^2 - k_1^2\right] \tag{6}$$

Therefore, an upper bound on the number of patterns than can be used is the ratio of the area of the annulus to the area of the filter (which represents how many none overlapping circles can be fit in the annulus:

$$2N \le \frac{A_{Annulus}}{A_{Filter}} = \frac{k_{diff}^2 - k_1^2}{k_{filter}^2} \tag{7}$$

The factor of two is due to the symmetry of the Fourier domain; specifically, the copying of information to both positive and negative frequency locations for a given modulation. Furthermore, this is an upper bound since it includes the gaps between the filling circles in the calculation. Hence,

Optics EXPRESS

$$\frac{2N}{k_{diff}^2 - k_I^2} \le \frac{1}{k_{filter}^2} \tag{8}$$

The resolution of the recovered image is determined by the size of the filter, due to the exclusion of high frequency image information outside of the filter region. Since, $k_{filter}^2 \propto D^{-2}$, where D is the smallest resolvable distance, then the limit on the resolution of the recovered image is:

$$D \ge \frac{\alpha N^{1/2}}{\left(k_{diff}^2 - k_I^2\right)^{1/2}} \tag{9}$$

where α is a constant. Hence, D will increase if the number of modulation patterns is increased, representing lower image quality for the recovered images. Furthermore, in order to decrease D, one must choose to use less patterns and larger filter radii.

5. Summary and conclusions

Single-shot nanosecond-resolution multiframe passive imaging method, Multiplexed Structured Imaging and Capture (MUSIC) was demonstrated to characterize avalanche ionization of laser-induced plasma in air. The MUSIC technique uses beamsplitters and optical delay lines to generate time evolution of a scene. On each beampath the image is uniquely coded by a Ronchi ruling, producing distinct spatial frequency shifts of the image in the spatial Fourier domain. The multiplexed images from individual beampaths are captured by a time-gated camera at a few nanoseconds. The final image, containing time evolution of the scene from each path, is demultiplexed in the after-processing to recover nanosecond-resolution images. The technique is used to monitor the temporal evolution of the avalanche ionization process in the laser-induced plasma in air. Comparisons with coherent microwave scattering measurements and plasma modeling yield good agreements.

The MUSIC technique as demonstrated here, is a passive imaging technique, which has the following characteristics:

1. The fundamental principle is to encode the time lapse into the spatial frequency domain using different spatial modulation patterns prior to arriving at the camera. Thus, a cumulative exposure can be captured in a single image, i.e., shifting the multiple exposures to various locations in the spatial frequency domain. Demultiplexing in the post-processing is achieved by homodyne mixing with the modulation pattern and low-pass filtering.

2. The spatial resolution of time-multiplexing images is reduced and controlled by the low-pass filter. It is inherently determined by the uncertainty principle of Fourier transformation, $\Delta f_r \cdot \Delta r \ge 1$.

3. The maximum multiplexing, i.e., maximum number of frames with maximum spatial resolutions, is obtained by fully occupying the frequency domain. It is corresponding to modulate the images with varying angles and cycle periods to fill the whole frequency domain up to the diffraction limit circle.

Overall, the ability to overlay multiple frames into a single image can be very beneficial in various applications where only a single camera is available (e.g., optical access restrictions). The MUSIC passive imaging technique can be useful for high temporal resolution applications in physics, chemistry and engineering.

Funding

NSF PHY-1418848; JDRD at University of Tennessee.

Optics EXPRESS

References

1. H. Mikami, L. Gao, and K. Goda, "Ultrafast optical imaging technology: principles and applications of emerging methods," in *Nanophotonics* (2016), p. 497.
2. T. G. Etoh, D. V. Son, T. Yamada, and E. Charbon, "Toward One Giga Frames per Second-Evolution of in Situ Storage Image Sensors," Sensors (Basel) **13**(4), 4640–4658 (2013).
3. T. G. Etoh, A. Q. Nguyen, Y. Kamakura, K. Shimonomura, T. Y. Le, and N. Mori, "The Theoretical Highest Frame Rate of Silicon Image Sensors," Sensors (Basel) **17**(3), 483 (2017).
4. G. P. Wakeham and K. A. Nelson, "Dual-echelon single-shot femtosecond spectroscopy," Opt. Lett. **25**(7), 505–507 (2000).
5. M. Linne, M. Paciaroni, T. Hall, and T. Parker, "Ballistic imaging of the near field in a diesel spray," Exp. Fluids **40**(6), 836–846 (2006).
6. S. P. Duran, J. M. Porter, and T. E. Parker, "Ballistic imaging of diesel sprays using a picosecond laser: characterization and demonstration," Appl. Opt. **54**(7), 1743–1750 (2015).
7. A. Velten, R. Raskar, D. Wu, B. Masia, A. Jarabo, C. Barsi, C. Joshi, E. Lawson, M. Bawendi, and D. Gutierrez, "Imaging the propagation of light through scenes at picosecond resolution," Commun. ACM **59**(9), 79–86 (2016).
8. G. Bub, M. Tecza, M. Helmes, P. Lee, and P. Kohl, "Temporal pixel multiplexing for simultaneous high-speed, high-resolution imaging," Nat. Methods **7**(3), 209–211 (2010).
9. J. Liang, L. Zhu, and L. V. Wang, "Single-shot real-time femtosecond imaging of temporal focusing," Light Sci. Appl. **7**(1), 42 (2018).
10. L. Gao, J. Liang, C. Li, and L. V. Wang, "Single-shot compressed ultrafast photography at one hundred billion frames per second," Nature **516**(7529), 74–77 (2014).
11. A. Ehn, J. Bood, Z. Li, E. Berrocal, M. Aldén, and E. Kristensson, "FRAME: femtosecond videography for atomic and molecular dynamics," Light Sci. Appl. **6**(9), e17045 (2017).
12. M. Gragston, C. D. Smith, and Z. Zhang, "High-speed flame chemiluminescence imaging using time-multiplexed structured detection," Appl. Opt. **57**(11), 2923–2929 (2018).
13. S. R. Khan, M. Feldman, and B. K. Gunturk, "Extracting sub-exposure images from a single capture through Fourier-based optical modulation," Signal Process. Image Commun. **60**, 107–115 (2018).
14. J. Liang and L. V. Wang, "Single-shot ultrafast optical imaging," Optica **5**(9), 1113–1127 (2018).
15. A. Braun, G. Korn, X. Liu, D. Du, J. Squier, and G. Mourou, "Self-channeling of high-peak-power femtosecond laser pulses in air," Opt. Lett. **20**(1), 73–75 (1995).
16. B. Dromey, M. Zepf, A. Gopal, K. Lancaster, M. Wei, K. Krushelnick, M. Tatarakis, N. Vakakis, S. Moustaizis, R. Kodama, M. Tampo, C. Stoeckl, R. Clarke, H. Habara, D. Neely, S. Karsch, and P. Norreys, "High harmonic generation in the relativistic limit," Nat. Phys. **2**(7), 456–459 (2006).
17. A. Dogariu, J. B. Michael, M. O. Scully, and R. B. Miles, "High-gain backward lasing in air," Science **331**(6016), 442–445 (2011).
18. M. B. Shattan, D. J. Miller, M. T. Cook, A. C. Stowe, J. D. Auxier, C. Parigger, and H. L. Hall, "Detection of uranyl fluoride and sand surface contamination on metal substrates by hand-held laser-induced breakdown spectroscopy," Appl. Opt. **56**(36), 9868–9875 (2017).
19. B. Sallé, J. L. Lacour, P. Mauchien, P. Fichet, S. Maurice, and G. Manhès, "Comparative study of different methodologies for quantitative rock analysis by Laser-Induced Breakdown Spectroscopy in a simulated Martian atmosphere," Spectrochim. Acta B At. Spectrosc. **61**(3), 301–313 (2006).
20. P. S. Hsu, M. Gragston, Y. Wu, Z. Zhang, A. K. Patnaik, J. Kiefer, S. Roy, and J. R. Gord, "Sensitivity, stability, and precision of quantitative Ns-LIBS-based fuel-air-ratio measurements for methane-air flames at 1-11 bar," Appl. Opt. **55**(28), 8042–8048 (2016).
21. P. S. Hsu, S. Roy, Z. Zhang, J. Sawyer, M. N. Slipchenko, J. G. Mance, and J. R. Gord, "High-repetition-rate laser ignition of fuel-air mixtures," Opt. Lett. **41**(7), 1570–1573 (2016).
22. Y. Wu, J. C. Sawyer, L. Su, and Z. Zhang, "Quantitative measurement of electron number in nanosecond and picosecond laser-induced air breakdown," J. Appl. Phys. **119**(17), 173303 (2016).
23. Z. Zhang, M. N. Shneider, and R. B. Miles, "Microwave diagnostics of laser-induced avalanche ionization in air," J. Appl. Phys. **100**(7), 074912 (2006).
24. Z. Zhang, M. N. Shneider, and R. B. Miles, "Coherent microwave rayleigh scattering from resonance-enhanced multiphoton ionization in argon," Phys. Rev. Lett 98, 265005 (2007).
25. D. L. Donoho, "Compressed sensing," IEEE Trans. Inf. Theory **52**(4), 1289–1306 (2006).
26. A. Perelomov and V. Popov, "Ionization of atoms in an alternating electric field," Sov. Phys. JETP **23**, 924–934 (1966).
27. J. Schwarz, P. Rambo, M. Kimmel, and B. Atherton, "Measurement of nonlinear refractive index and ionization rates in air using a wavefront sensor," Opt. Express **20**(8), 8791–8803 (2012).
28. V. D. Mur, S. V. Popruzhenko, and V. S. Popov, "Energy and momentum spectra of photoelectrons under conditions of ionization by strong laser radiation (The case of elliptic polarization)," J. Exp. Theor. Phys. **92**(5), 777–788 (2001).

218.96.202.123 {ts '2019-07-31 17:22:07'}